ARTICLES
https://doi.org/10.1038/s41565-021-00875-7
nature nanotechnology

Check for updates

A highly homogeneous polymer composed of tetrahedron-like monomers for high-isotropy expansion microscopy

Ruixuan Gao[1,2,3,17], Chih-Chieh (Jay) Yu[1,2,4,17], Linyi Gao[2,4,5], Kiryl D. Piatkevich[1,2], Rachael L. Neve[6], James B. Munro[7], Srigokul Upadhyayula[3,8,9,10,11,12] and Edward S. Boyden[1,2,4,13,14,15,16] ✉

Expansion microscopy (ExM) physically magnifies biological specimens to enable nanoscale-resolution imaging using conventional microscopes. Current ExM methods permeate specimens with free-radical-chain-growth-polymerized polyacrylate hydrogels, whose network structure limits the local isotropy of expansion as well as the preservation of morphology and shape at the nanoscale. Here we report that ExM is possible using hydrogels that have a more homogeneous network structure, assembled via non-radical terminal linking of tetrahedral monomers. As with earlier forms of ExM, such 'tetra-gel'-embedded specimens can be iteratively expanded for greater physical magnification. Iterative tetra-gel expansion of herpes simplex virus type 1 (HSV-1) virions by ~10× in linear dimension results in a median spatial error of 9.2 nm for localizing the viral envelope layer, rather than 14.3 nm from earlier versions of ExM. Moreover, tetra-gel-based expansion better preserves the virion spherical shape. Thus, tetra-gels may support ExM with reduced spatial errors and improved local isotropy, pointing the way towards single-biomolecule accuracy ExM.

Expansion microscopy is in increasingly widespread use for biological imaging because it enables, via physical magnification of the specimen[1–3], nanoscale imaging on conventional, ubiquitous optical microscopes. In ExM, biological specimens are densely permeated by a swellable hydrogel. Biomolecules and/or fluorescent tags are covalently anchored to the hydrogel network, the specimen is chemically softened, and the hydrogel is expanded upon immersion in water (typically ~4.5× in linear dimension). Protocols using off-the-shelf-chemicals[4] have helped ExM find utility in a wide variety of contexts, ranging from the mapping of ribosome components and RNAs in synaptic compartments[5], to the analysis of circadian rhythm neural circuitry in the *Drosophila* brain[6], to the analysis of cancer in human biopsies[7]. Variants of ExM have been developed that achieve nanoscale localization of proteins and RNAs in preserved cells and tissues on diffraction-limited microscopes[4,7–13]. In addition, multiple strategies have been introduced to expand specimens ~10–20×, including applying the expansion process repeatedly (iterative expansion microscopy, or iExM)[14] or by using superabsorbent hydrogels (X10 expansion microscopy)[15]. However, all ExM variants so far form the hydrogel mesh via free-radical chain-growth polymerization, a process that results in nanoscale structural heterogeneity in the hydrogel network[16–20]. This raises the question of whether another polymer might provide better structural homogeneity, and thus less spatial error, during the expansion process.

To provide context we describe two earlier ExM protocols. One popular version of ExM is protein-retention expansion microscopy (proExM)[8]. First, fixed biological specimens labelled with fluorophore-conjugated antibodies are exposed to a small molecule (acryloyl-X, SE, the succinimidyl ester of 6-((acryloyl) amino)hexanoic acid) that attaches a polymerizable acryloyl group to primary amine groups on antibodies and endogenous proteins. The specimen is then immersed in a solution containing sodium acrylate and acrylamide, as well as the cross-linker *N*,*N*′-methylenebisacrylamide, to form a dense network of cross-linked sodium polyacrylate/polyacrylamide hydrogel (PAAG) throughout the specimen. During the polymerization, antibodies and proteins are covalently anchored to the hydrogel via acryloyl-X, SE. Finally, proteinase K treatment cleaves most of the proteins, largely sparing the antibody-conjugated fluorophores, allowing expansion of the polymer-specimen composite in water. As a second example, in iExM[14], fixed specimens are labelled first with primary antibodies and then with DNA oligonucleotide-conjugated secondary antibodies. Next, DNA oligonucleotides bearing a gel-anchorable moiety are hybridized to the secondary antibody-conjugated DNA oligonucleotides. Then a first hydrogel is formed as above, which anchors the gel-anchorable DNA oligonucleotides to the hydrogel at the locations of the immunostained proteins; this gel is made with a cleavable cross-linker. Subsequently, this gel is expanded as described above. Next, another round of hybridization of DNA oligonucleotides that are complementary to those anchored to the first hydrogel, and again bearing a gel-anchorable moiety, is performed. Then, a second hydrogel is formed throughout the expanded first

[1]McGovern Institute for Brain Research, MIT, Cambridge, MA, USA. [2]Media Arts and Sciences, MIT, Cambridge, MA, USA. [3]Janelia Research Campus, Howard Hughes Medical Institute, Ashburn, VA, USA. [4]Department of Biological Engineering, MIT, Cambridge, MA, USA. [5]Broad Institute, MIT, Cambridge, MA, USA. [6]Department of Neurology, Massachusetts General Hospital, Cambridge, MA, USA. [7]Department of Microbiology and Physiological Systems, University of Massachusetts Medical School, Worcester, MA, USA. [8]Department of Cell Biology, Harvard Medical School, Boston, MA, USA. [9]Program in Cellular and Molecular Medicine, Boston Children's Hospital, Boston, MA, USA. [10]Department of Pediatrics, Harvard Medical School, Boston, MA, USA. [11]Advanced Bioimaging Center, University of California at Berkeley, Berkeley, CA, USA. [12]Department of Molecular and Cell Biology, University of California at Berkeley, Berkeley, CA, USA. [13]MIT Center for Neurobiological Engineering, MIT, Cambridge, MA, USA. [14]Department of Brain and Cognitive Sciences, MIT, Cambridge, MA, USA. [15]Koch Institute, MIT, Cambridge, MA, USA. [16]Howard Hughes Medical Institute, Cambridge, MA, USA. [17]These authors contributed equally: Ruixuan Gao, Chih-Chieh (Jay) Yu. ✉e-mail: edboyden@mit.edu

hydrogel so that the new DNA oligonucleotides are anchored to the second hydrogel at the original sites of immunostained proteins. Finally, the first hydrogel is cleaved, allowing the second hydrogel to expand upon immersion in water. The protein locations can be imaged after the polymer-anchored oligonucleotides are labelled by applying complementary oligonucleotides, potentially equipped with branched DNA for amplification purposes, bearing fluorescent dyes. In short, the oligonucleotides provide a molecular mechanism (based on complementary strand hybridization) for signal transfer between the first and second hydrogels, as well as a scaffold for amplification and fluorescence readout.

In both cases, the free-radical chain-growth polymerization process that forms the PAAG has nanoscale structural heterogeneity. The size of local cross-linker density variations (Fig. 1a, '1') can amount to 15–25 nm for thus-synthesized polyacrylamide gels[16]. Topological defects, such as dangling ends (Fig. 1a, '2') and loops (Fig. 1a, '3'), can introduce deviations from uniform polymer meshes at the 1–10 nm length scale[19,20]. So far, many attempts have been made to obtain a more ideal hydrogel matrix[19–24]. One strategy has been to adopt step-growth polymerization. For example, photoinitiated thiol-ene step-growth polymerization formed a more homogeneous network structure versus that yielded by chain-growth polymerization[25–27]. In another strategy, terminal linking of two kinds of tetrahedral poly(ethylene glycol) (PEG) monomer has been utilized to form a diamond lattice-like polymer network[19,20,24]. The hydrogel thus formed, via non-radical step-growth polymerization, known as a tetra-PEG gel, approximates an ideal polymer network that is nearly void of structural defects, both as synthesized and when slightly swollen (<1.5× linear expansion in water)[28,29]. The tetra-PEG gel structure has been further extended to create hydrogels with versatile chemical and mechanical properties, including polyelectrolyte hydrogels[30] and highly compressible and stretchable hydrogels[31].

Here we report an ExM methodology using swellable hydrogels assembled by click-chemistry-based, non-radical linking of two complementary, tetrahedral monomers comprising backbones of polyacrylate and PEG respectively, which we call a tetra-gel (TG). TG-expanded herpes simplex virus type 1 (HSV-1) virions exhibited envelope shapes with substantially smaller spatial errors (9.2 nm of deviation) compared with classical PAAG-expanded virions (14.3 nm). As a result of these reduced spatial errors, TG-based ExM better preserves the spherical shapes of the virions compared with PAAG-based ExM. Thus, the TG serves as a candidate for a more structurally homogeneous ExM matrix compared with that synthesized by free-radical chain-growth polymerization, and points towards new ways of improving and extending the ExM toolbox.

Design of the TG structure and assembly mechanism

We designed and synthesized tetrahedral monomers closely related to those used for tetra-PEG gels (Fig. 1b)[24,28–30]. One monomer (**1**) has a tetra-arm polyacrylate backbone with a clickable terminal azide group (synthesis and NMR spectra in Supplementary Figs. 1 and 2, respectively); the other monomer (**2**) has a tetra-arm PEG backbone with a complementary terminal alkyne group. The alkyne was varied to tune the reactivity of the terminal linking and functionality of the hydrogel (Fig. 1b, monomers **2′**, **2″** and **2‴**). The monomers have comparable molecular weights of ~10–20 kDa and an arm length of ~3–6 nm at the gelation step (at an ionic strength of ~0.150 M). In the solution phase, monomer **1** has four negatively charged polyacrylate arms ($n \approx 21$ acrylate units), each arm of which is estimated to extend ~4.0–5.7 nm, based on the previously characterized persistence length of ≥4.0 nm (ref. [32]) and the fully stretched length of ~5.7 nm. Monomer **2** has four uncharged PEG arms ($n \approx 57$ or $n \approx 114$ ethylene glycol units, depending on which version is used), each of which has a fully stretched length of ~21.7 or ~43.3 nm, respectively, which greatly exceeds its persistence length of 0.38 nm[33]. The PEG arm can thus be modelled as a freely jointed chain in solution[34,35], whose root-mean-square (r.m.s.) arm length can be calculated as ~2.9 or ~4.1 nm, respectively. For the synthesis of monomer **2**, the $n \approx 57$ backbone was used for variants **2′** and **2″** and the $n \approx 114$ backbone was used for variant **2‴**. The increased number of ethylene glycol units in **2‴** enhanced its solubility, compensating for the hydrophobic nature of the disulfide-dibenzocyclooctyne (SS-DBCO) moiety. Finally, when monomer **1** and a selected monomer **2** are mixed, a hydrogel forms via click-chemistry-based terminal linking (Fig. 1c, left). Then, in water or aqueous buffers with an ionic strength of $\lesssim$0.05 M (the concentration estimated from Debye–Hückel theory for the electrostatic potential energy in electrolyte solutions)[36], the hydrogel swells due to the reduced electrostatic screening of salt ions between the mutually repelling monomer **1** units (~84 negative charges per monomer), which in turn elongates the originally unstructured PEG arms of the interconnecting monomer **2** (Fig. 1c, right).

Of the monomer **2** variants in Fig. 1b, the bicyclononyne (BCN) version (monomer **2″**) was designed to support the expansion of thicker specimens, because its slower click-reaction kinetics (by ~55% versus standard DBCO)[37] provide additional time for the monomers to equilibrate in concentration throughout the tissues during pre-gelation incubation. In addition, a slower gelation reaction[38] has been demonstrated to increase the homogeneity of the polymer network. Indeed, gelation occurs in ~1 and ~2.5 h at 4 °C for monomers **2′** and **2″**, respectively. The SS-DBCO version (monomer **2‴**) supports post-expansion cleavage of the polymer network into individual monomers, rendering it compatible with iterative expansion[14]. Monomer **2‴**-based gelation takes ~4 h at 4 °C, again suggesting its utility for thicker specimens.

TG expansion of cells and tissues

We mixed monomers **1** and **2** in a 1:1 ratio (although small deviations may occur depending on the exact fraction of monomer **1** whose *t*-butyl group was removed in the final step of its synthesis; Supplementary Fig. 1, bottom row); the gelling solution was then cast into a circular mould. Notably, deviation from a 1:1 ratio would result in additional defects in the polymer network and thus an increase in the structural heterogeneity[28]. Using a virion-based local expansion isotropy assay (described later), we observed growing discrepancies versus the ground-truth virion size when the monomer ratio deviated from 1:1 (Supplementary Fig. 3). After 1–2 h of incubation at 37 °C, the gelling solution solidified into an optically transparent and mechanically elastic hydrogel (Fig. 2a, left). Similar to the PAAG gel and other types of hydrogel used in ExM that are formed by free-radical chain-growth polymerization[7–13], the gel swelled (approximately threefold in the linear dimension) after salt elution in water (Fig. 2a, right). Fluorescently labelled gels (Fig. 2b) showed the linear expansion factor to be ~3.0–3.5×.

Next, we implemented proExM using TG. We infused antibody-stained cells and tissue slices with NHS-azide (NHS = *N*-hydroxysuccinimide) to link proteins and antibodies (via primary amines) to the polymer network through click chemistry (Fig. 1b). We then formed the TG in situ, followed by the addition of proteinase K and swelling in water. In one implementation, HEK cells were immunostained with antibodies against microtubules and then processed using the DBCO version (monomer **2′**) of the TG. Water swelled the HEK cell–TG composite ~2.9-fold, resulting in more sharply resolved microtubules than could be seen before expansion using the same diffraction-limited confocal microscope (Fig. 2c). We aligned the pre- and post-expansion confocal microscopy images of the microtubules via non-rigid registration and quantified the amount of distortion in the expansion process (Fig. 2d), finding ~2.5% error over lengths of ~20 μm, comparable to that of PAAG-based proExM[1,8]. In another implementation, mouse brain slices expressing yellow fluorescent protein (YFP), processed

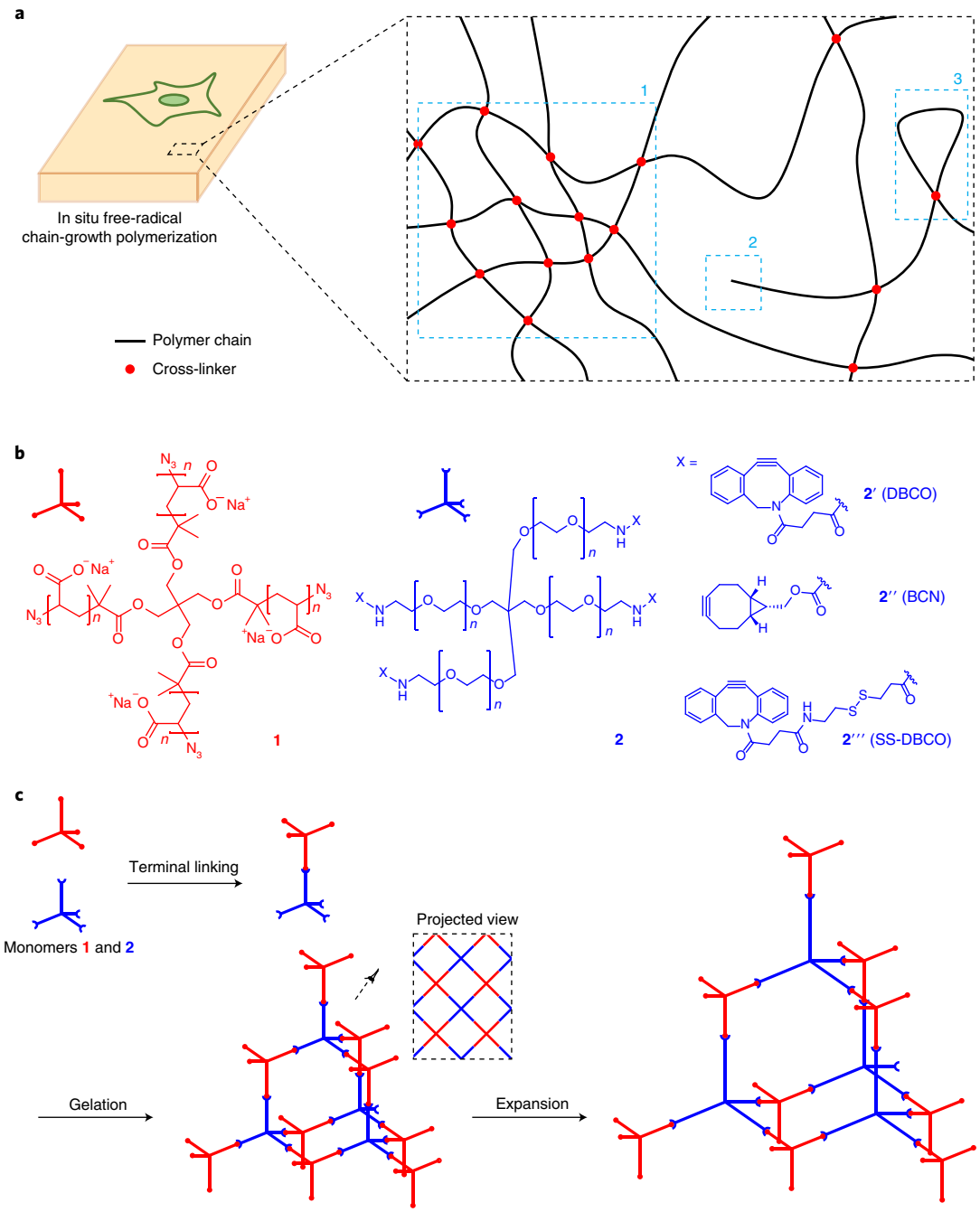

Fig. 1 | Design and synthesis of the tetra-gel (TG) for ExM. a, Cell/tissue–hydrogel composites formed by in situ free-radical chain-growth polymerization are known to have structural inhomogeneities in the range of tens of nanometres due to (1) local fluctuations of monomer and cross-linking densities, (2) dangling ends and (3) loops formed within the polymer network. **b**, Design of the TG monomers **1** and **2** with tetrahedral symmetry and reactive terminal groups. Specific monomer **2** terminal groups (**2′**, **2″** and **2‴**) enable, for example, control of the reaction rate between the monomers and the addition of functionalities to the polymer network. **c**, Formation and expansion of the TG via click-chemistry-based terminal linking of monomers **1** and **2**. Inset: projected view of the TG polymer network.

using the BCN version (monomer **2″**) of the TG, after immunostaining against YFP to enhance the fluorescence (Fig. 2e), expanded ~3.0-fold and showed excellent detail in structures such as dendritic spines, as seen with PAAG-based proExM[8].

Since the TG is formed via non-radical polymerization, TG-based expansion could potentially preserve molecules that are inactivated during free-radical chain-growth polymerization. We found that the fluorescence of dyes known to be inactivated by PAAG-based proExM[8] (Fig. 2f), including Alexa Fluor 647 (AF647), Cy5 and Alexa Fluor 680 (AF680), was largely retained after TG-based expansion (Fig. 2f,g). Thus TG-based ExM may preserve molecules not compatible with PAAG-based ExM.

TG-based iterative expansion

The SS-DBCO version of the TG (using monomer **2‴**) would allow the TG polymer network to be cleaved at each network node (Fig. 3a), as appropriate for iExM[14]. Indeed, we found that HeLa cells, when expanded with TG, could be iteratively expanded (Fig. 3b).

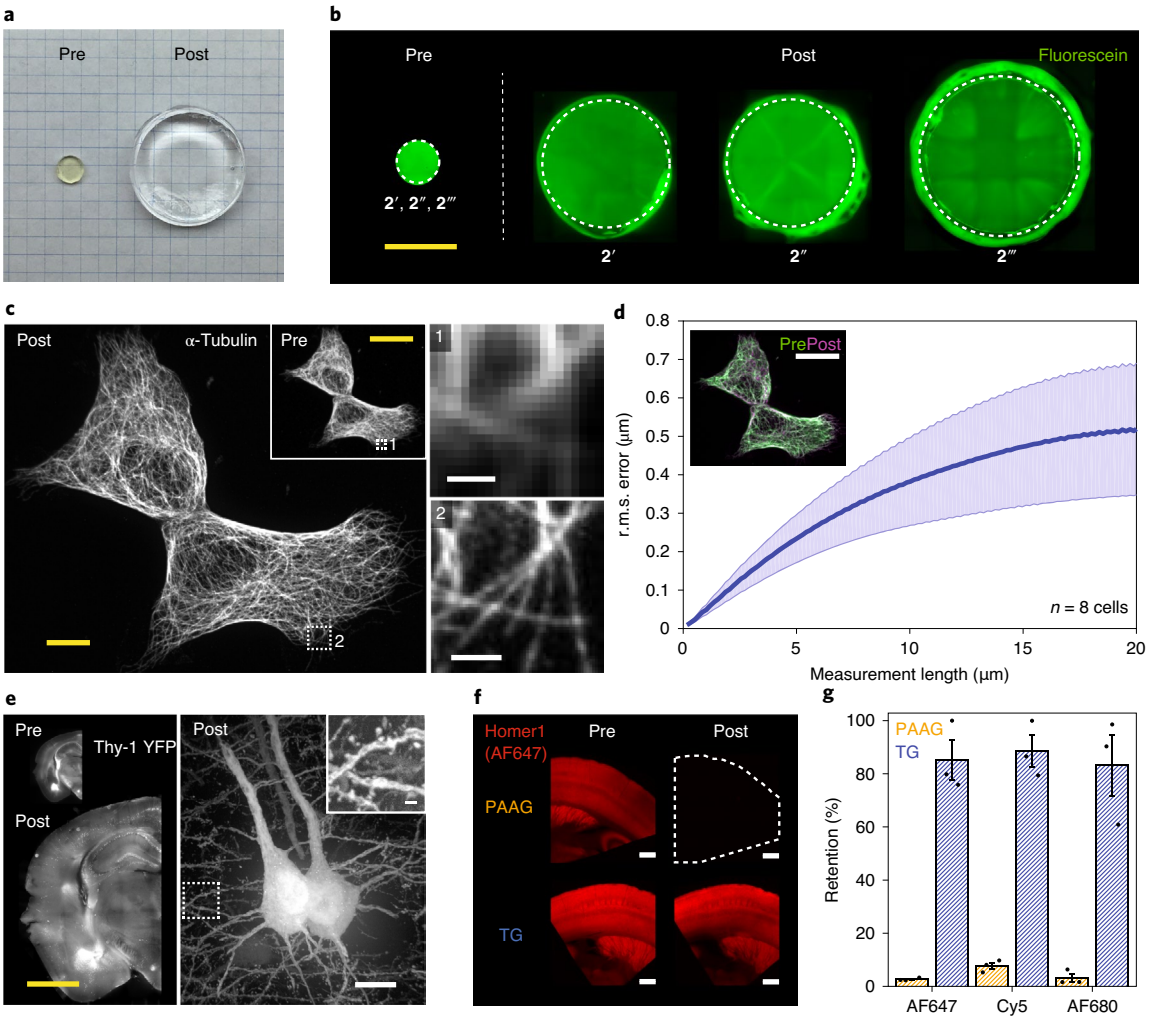

Fig. 2 | TG-mediated expansion of cells and tissues. a, Image of the TG (using monomer **2‴**) as synthesized (left, pre-expansion) and after swelling in deionized water (right, post-expansion). The two gels were cast in circular moulds with identical dimensions. Grid size, 5 mm. **b**, TG labelled with fluorescein in the pre-expansion state (left, **2′**; the same sizes and shapes were obtained when **2″** and **2‴** were used) and the post-expansion state (right, **2′**, **2″** and **2‴**). Irregular boundaries on the post-expansion images reflect the meniscus of water used to expand the gels. Scale bar, 5 mm. **c**, Left, HEK293 cells with α-tubulin immunostaining in pre- (inset) and post-expansion states. Expansion factor, 2.85×. Scale bars, 20 μm. Right, magnified views of the boxed regions 1 (top) and 2 (bottom). Scale bars, 1 μm (2.85 μm). (Here and after, unless otherwise noted, the scale bar sizes are provided at the pre-expansion scale (that is, the biological scale) with the corresponding post-expansion size (that is, the physical size) indicated in parentheses.) Results are representative of five cells from the same cell culture. **d**, The r.m.s. error curve for HEK293 cell expansion (blue line, mean; shaded area, standard deviation; $n = 8$ cells from one culture). Inset: non-rigidly registered and overlaid pre- (green) and post-expansion (magenta) images used for the r.m.s. error analysis. Scale bar, 20 μm (57 μm). **e**, Pre- (left top) and post-expansion (left bottom and right) Thy1-YFP mouse brain slices. Expansion factor, 3.00×. Scale bars, 5 mm (left) and 10 μm (right, 30 μm). The gelled brain slice in the lower left panel was immunostained against yellow fluorescent protein (YFP) after the proteolysis step to enhance the fluorescence. Inset: magnified view of the boxed region. Scale bar, 1 μm (3 μm). Results are representative of two slices from the same single batch of brain slice preparation for each panel. **f**, Pre-expansion (left column) and post-expansion (right column) Thy1-YFP mouse brain slices immunostained with Homer1 primary antibody and AF647-conjugated secondary antibody, using PAAG (top row) and TG (bottom row). Expansion factor, 3.93× (PAAG) and 2.72× (TG). Scale bars, 300 μm (top right, 1.18 mm; bottom right, 815 μm). Results are representative of three slices from the same single batch of brain slice preparation for each gel type. **g**, Fluorescence retention of AF647, Cy5 and AF680 with PAAG and TG in immunostained mouse brain slices processed as in **f** (bar height, mean; black dots, individual data points; error bar, standard error of the mean; $n = 3$ brain slices from one mouse).

We used a free-radical-chain-growth-polymerized gel for the second round of iExM, reasoning that the spatial errors introduced by the second-round expansion would be negligible compared with those introduced by the first round (since, when considered in biological units, that is, in terms of the relative spacing of biomolecules with respect to each other, second-round errors are effectively divided by the expansion factor of the first round). TG-based iExM expanded the cells by approximately 16-fold, revealing the hollow structure of the microtubules (Fig. 3c), with a sidewall separation comparable to that seen previously with iExM of BS-C-1 cells using PAAG-based iExM (Fig. 3d). We note that, compared with that observed, for example, by STORM (stochastic optical reconstruction microscopy), the larger sidewall distance seen here can be explained by the label size effect described previously—classical iExM requires larger labels than used in other super-resolution methods[14]. Finally, multiple DNA oligonucleotide-conjugated antibodies could be used at

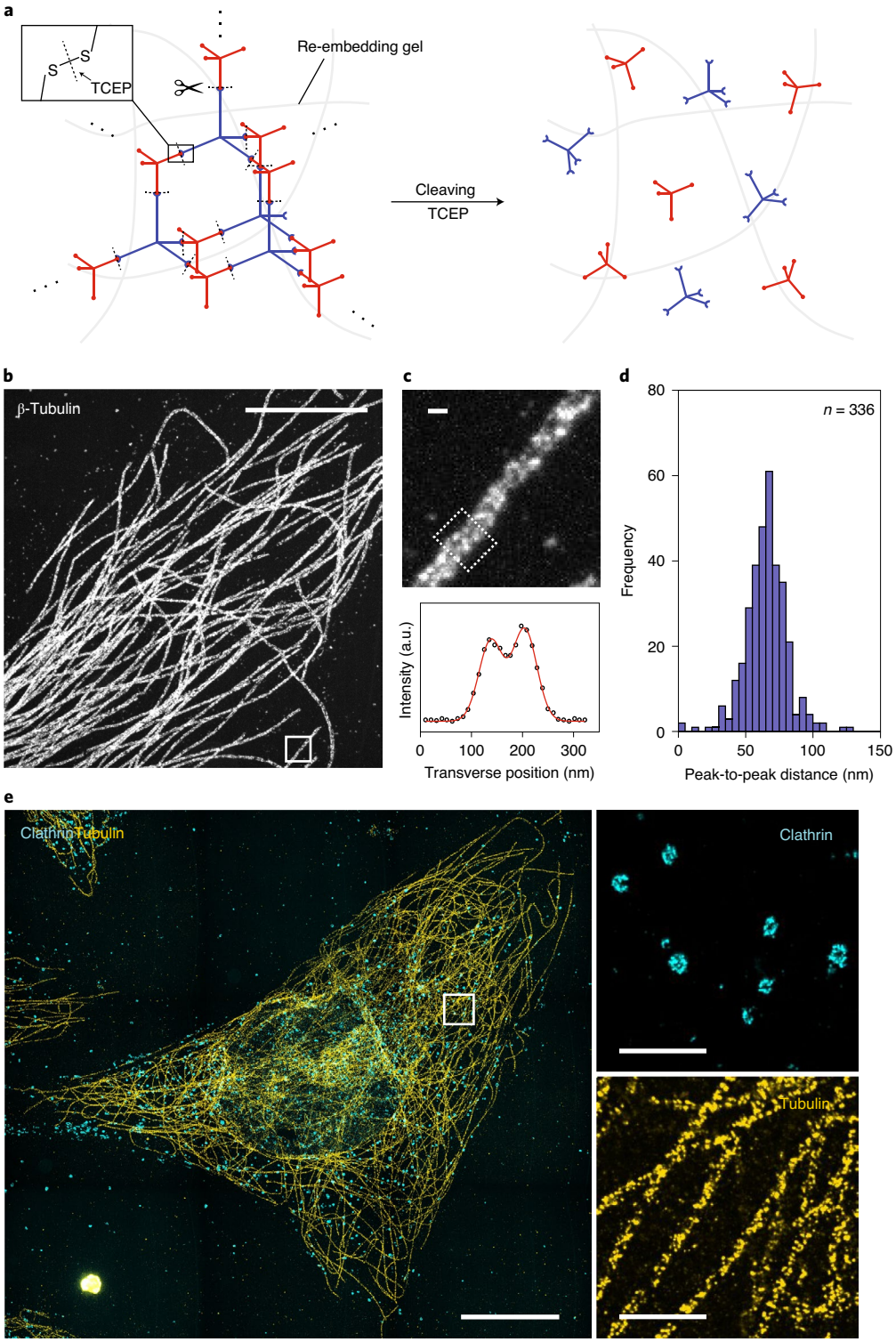

Fig. 3 | TG-based iterative expansion. a, Monomeric cleaving of TG (monomer **2**‴) after re-embedding in a second hydrogel. A reducing agent, tris(2-carboxyethyl)phosphine (TCEP), was applied to cleave the disulfide bonds in the TG polymer network. **b**, HeLa cell with β-tubulin immunostaining, expanded by cleavable TG-based two-round iterative expansion. Expansion factor, 15.6×. Scale bar, 5 μm (78.2 μm). Results are representative of ten cells from the same cell culture. **c**, Top, magnified view of the boxed region in **b**. Scale bar, 100 nm (1.56 μm). Bottom, transverse line intensity profile of the microtubule in a single *xy* plane in the dashed box (circle points) and the fitted sum of two Gaussians (red line). The line intensity profile was averaged in the direction parallel to the microtubule axis over a length of 200 nm. **d**, Histogram of peak-to-peak distance between microtubule sidewalls in HeLa cells ($n = 336$ segments of a length of 200 nm from ten cells in one culture). **e**, Left, HeLa cell with two-colour labelling of clathrin-coated pits/vesicles and microtubules, expanded by TG-based two-round iterative expansion. Expansion factor, 15.6×. Scale bar, 10 μm (156 μm). Right, magnified view of the boxed region for each colour channel. Scale bars, 1 μm (15.6 μm). Results are from one cell from the same cell culture preparation as in **b**.

once, for example, to label tubulin and clathrin in the TG-expanded HeLa cells (Fig. 3e)[14].

Spatial analysis of the TG-based ExM expansion error

To assess the spatial errors introduced by TG-based iExM, we imaged the nanoscale arrangement of virion envelope proteins. To minimize the label size effect mentioned above, we developed a direct, non-specific labelling strategy that targets primary amines of virus envelope proteins and reduces the label size from ~21 nm (ref. [14]) to that of a single DNA oligonucleotide (~7 nm). First, we directly conjugated 22-base-pair oligonucleotides to the envelope proteins on the virions via a hydrazone-based DNA-to-peptide conjugation (Fig. 4a). We were careful not to expose viruses to any buffers containing detergents, for all steps from fixation to gelation, aiming to preserve the integrity of the virion's lipid bilayer envelope and directing the majority of the labelling to accessible envelope proteins on the outside of the membrane. HSV-1 virions have a well-defined envelope protein layer that has been characterized by methods such as electron microscopy[39–41], electron tomography[42,43] and super-resolution microscopy[44], and they have an appropriate length scale (170–190 nm diameter)[44], with features in the tens of nanometres, for characterizing the local homogeneity of the TG. After direct labelling of the envelope proteins, we then expanded the HSV-1 virions with TG-based iExM versus PAAG-based iExM (in both cases using PAAGs in the second round; Fig. 4b). We noted that this protocol was compatible with dual-colour labelling and imaging of envelope proteins and DNA (Supplementary Fig. 4) and could be applied to other types of enveloped viruses, such as the vesicular stomatitis virus (VSV), which is an RNA virus (Supplementary Fig. 5), and the human immunodeficiency virus (HIV), which is a retrovirus (Supplementary Fig. 6). For the quantitative analysis of envelope shapes, to gauge the TG-based iExM spatial error, we focused on viruses that have a spherical geometry (that is, HSV-1[42,43] and HIV[45]).

The expansion factor for TG-based iExM of the HSV-1 virions was ~10.3–13.3, and for PAAG-based iExM it was ~15.3–18.7. TG-based iExM appeared to result in more spherical virions than PAAG-based iExM (Fig. 4c). From single-particle averaged virion images, we found that the envelope protein profile of the TG-expanded HSV-1 virions was substantially sharper than that for the PAAG-expanded virions (Fig. 4d). Similarly, the TG-expanded HIV virions had sharper envelope profiles than the PAAG-expanded ones (Fig. 4e).

To quantify the spatial errors associated with each expansion process, we measured the standard deviation of the virion radius (σ) within the midplane of individual HSV-1 virions (Fig. 4f; computed in biological units, that is, normalized by the expansion factor, to compensate for the different expansion factors of the TG- and PAAG-based iExM protocols). The TG-expanded HSV-1 virions [σ_m (median σ across virions) = 9.2 nm; n = 352 virions; virions from a single batch of live HSV-1 preparation] had a significantly smaller σ_m value compared with the PAAG-expanded HSV-1 virions (σ_m = 14.3 nm; n = 330 virions; virions from the same single batch of live HSV-1 preparation; $p = 2.4 \times 10^{-24}$, two-sided Wilcoxon rank sum test; Fig. 4g). We calculated the same metric of σ for the single-particle averaged images of the HSV-1 virions (Fig. 4d) and saw smaller spatial errors for the TG-expanded virions [σ_a (σ of the averaged virion image) = 3.4 nm] compared with the PAAG-expanded ones (σ_a = 4.0 nm); note that the absolute difference between the two σ_a values was numerically small because of population averaging. HIV virions have much sparser envelope proteins per virion than HSV-1 virions, which precludes computing σ at the individual particle level; however, for single-particle averaged images, the TG-expanded HIV virions (σ_a = 8.9 nm) had a smaller σ_a value than the PAAG-expanded ones (σ_a = 12.9 nm), showing again the reduced spatial errors for TG-based iExM (Fig. 4e).

We made a unifying computational model so that different measures of hydrogel-based variability could be compared. We took the spatial errors calculated across individual particles (Fig. 4g) as the gold-standard metrics of spatial error, and sought to examine whether or not other metrics, such as those derived from single-particle averaged images (Fig. 4d,e), were consistent. For the model, we considered both chemical variability (for example, the hydrogel-associated local anisotropy) and biological variability (for example, the biological distribution of virion size). We developed a computational model that simulated the averaged images from individual simulated virions (Supplementary Methods and Supplementary Fig. 7). When single-particle averaged images were simulated based on this model, we observed sharper envelope profiles for TG than PAAG, consistent with the experimental results (Supplementary Fig. 7). Moreover, the metrics derived from the

Fig. 4 | Spatial errors introduced by TG-based versus classical PAAG-based iterative expansion. a, Short DNA oligonucleotides (22 base pairs) were covalently conjugated to the envelope proteins of HSV-1 virions via hydrazone formation, which allows labelling transfer across multiple hydrogels, amplification based on branched DNA, and fluorescence readout based on the hybridization of fluorescent oligonucleotides. **b**, Schematic illustration of TG- (top) and PAAG-based (bottom) iterative expansion of HSV-1 virions with the direct oligonucleotide-conjugation as in **a**. PAAG-based re-embedding and expansion was used for all expansion rounds after the first round, based on the reasoning that most of the error of an iterative expansion protocol is introduced in the first round of expansion (see text for details). **c**, HSV-1 virions with directly labelled envelope proteins, expanded by TG- (left) and PAAG-based (right) two-round iterative expansion. Scale bar (for both panels), 1 µm (TG, 10.3 µm; PAAG, 15.3 µm). Expansion factor, 10.3× (TG) and 15.3× (PAAG). Results are representative of three separately acquired fields of view from a single hydrogel preparation for each gel type, using virions from the same single batch of live HSV-1 preparation. **d**, Single-particle averaged images of HSV-1 virions after TG (top)- and PAAG-based (bottom) two-round iterative expansion (TG, n = 396; PAAG, n = 362 virions; virions from the same single batch of live HSV-1 preparation). Full width half maximum measurements of the radial intensity profile (the line intensity profile from the particle centre to the edge of the particle), 73.6 nm (TG) and 91.0 nm (PAAG). Scale bars, 100 nm. **e**, Single-particle averaged images of HIV virions expanded by TG- (top) and PAAG-based (bottom) two-round iterative expansion (TG, n = 61; PAAG, n = 73 virions; virions from the same single batch of live HIV preparation). Full width half maximum measurements of the radial intensity profile, 49.1 nm (TG) and 119.0 nm (PAAG). Scale bars, 100 nm. **f**, Top left and middle, representative single xy-plane images of HSV-1 virions expanded by TG- and PAAG-based two-round iterative expansion. White dashed lines indicate the eight directions along which the virion radius (R) was measured. Scale bars, 100 nm. Top right, representative line intensity profile (circle points) along a single direction (Direction 1) of the TG-expanded virion and the fitted Gaussian (red line). The distance from the centre of the Gaussian to the centre of the virion was defined as R along that direction. Bottom, histograms of the particle-mean-normalized R (R_n) for all measured line profiles [TG, n = 1,977; PAAG, n = 1,889 profiles; from 352 (TG) and 330 (PAAG) virions from the same single batch of live HSV-1 preparation]. **g**, Standard deviation (σ) of HSV-1 virion radius (R) within individual virions for TG- and PAAG-based iterative expansion ($p = 2.4 \times 10^{-24}$, two-sided Wilcoxon rank sum test; TG, n = 352; PAAG, n = 330 virions; virions from the same single batch of live HSV-1 preparation). Data are presented as box plots, where the ends of the whiskers represent the maximum and minimum values of the distribution after outlying points (values above the 75th percentile + 1.5 × interquartile range, or below the 25th percentile − 1.5 × interquartile range) have been excluded, and where the upper line of the box represents the 75th percentile, the middle line represents the 50th percentile (median), the lower line represents the 25th percentile and the plus signs represent the individual values of the outlying points.

simulated images were comparable to the experimental values to a great extent, despite the highly simplified assumptions and designs of the model.

To assess how the improved accuracy of TG- versus PAAG-based expansion helps to preserve the shapes of nanoscale objects like viruses, we characterized the expanded HSV-1 virion

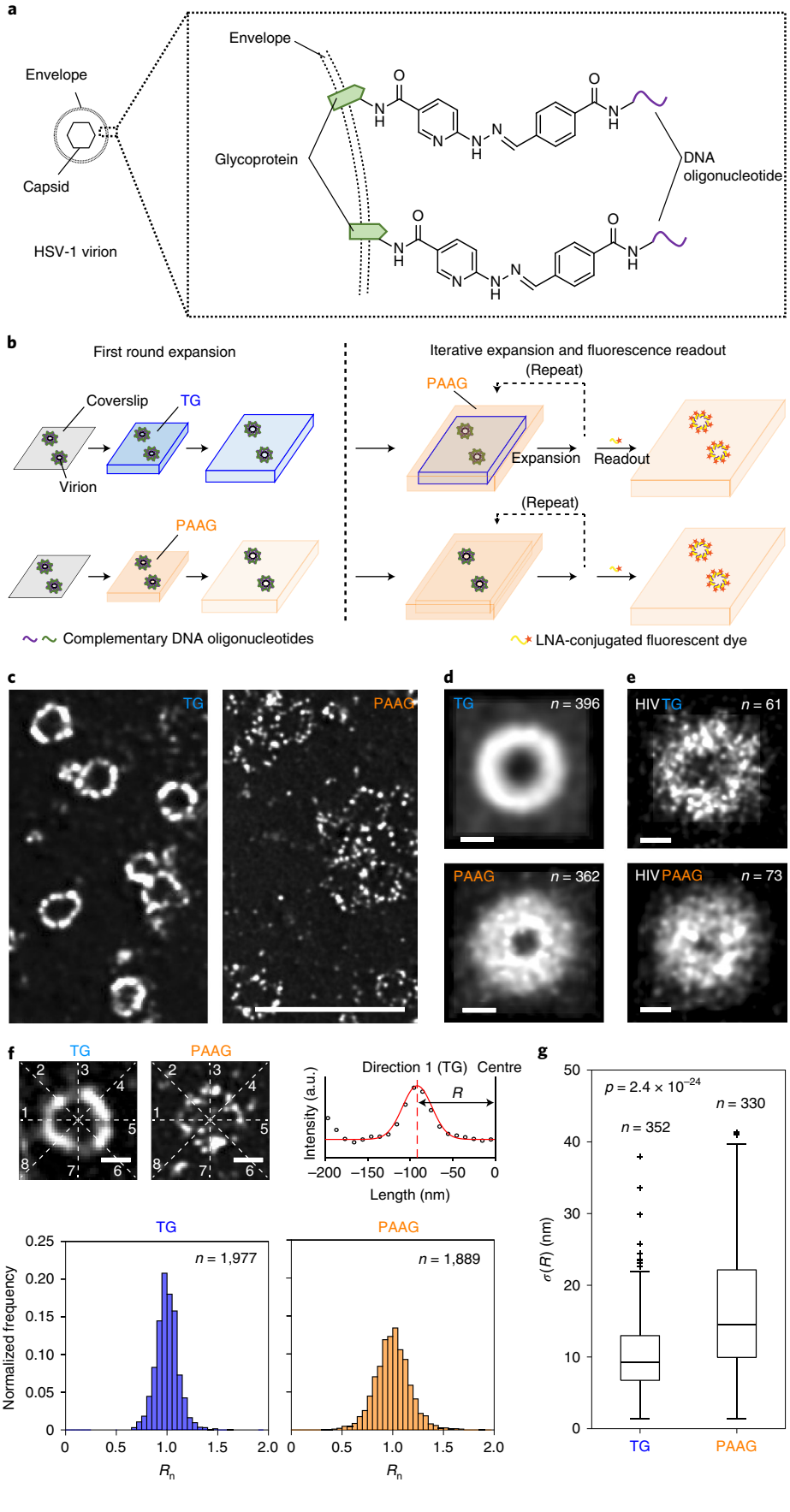

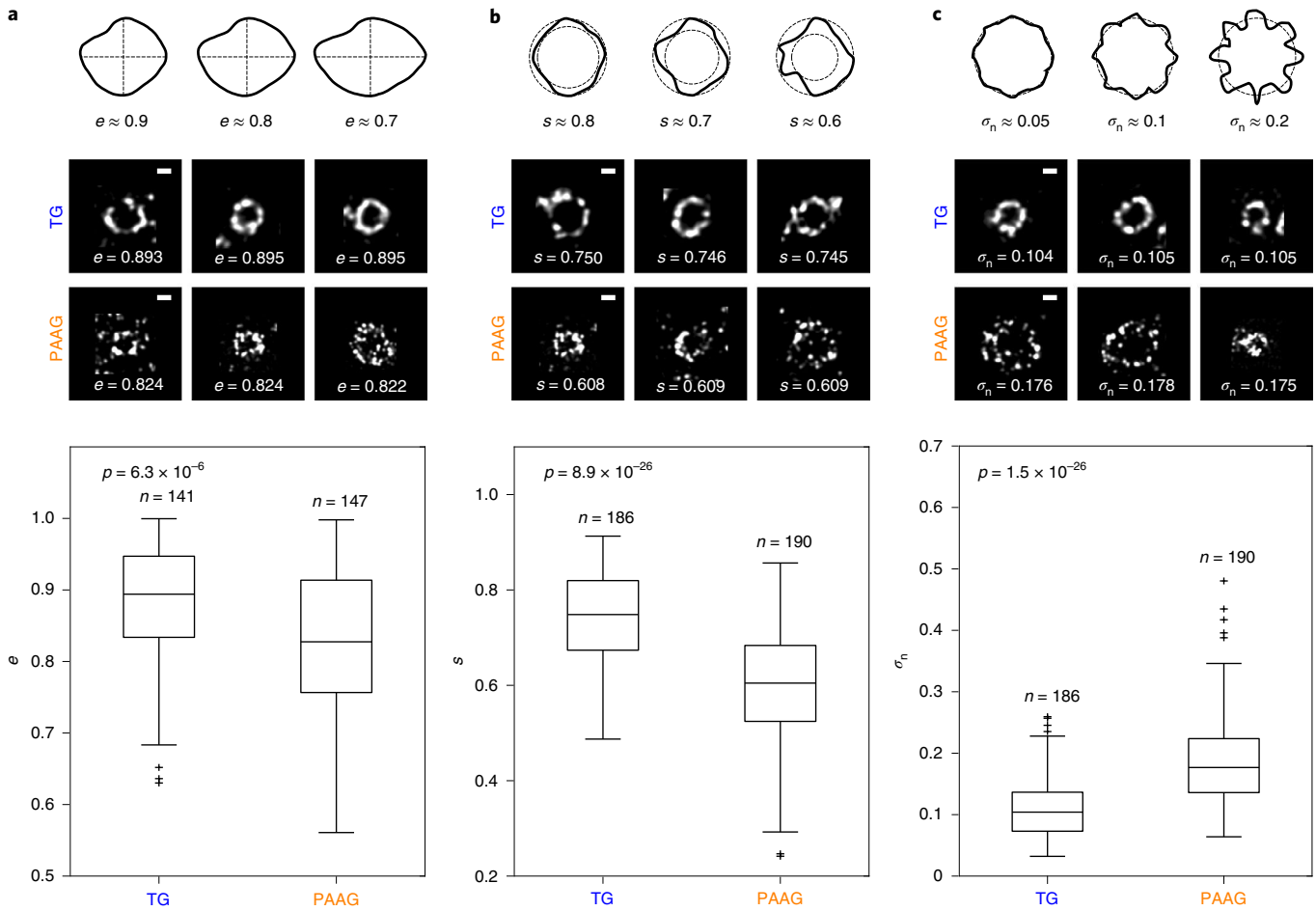

Fig. 5 | Shape analysis of TG- versus PAAG-expanded HSV-1 virions. a, Top, schematic examples of shapes with eccentricity (*e*) values of ~0.9, 0.8 and 0.7. Middle, HSV-1 virions expanded by TG- (top row) and PAAG-based (bottom row) two-round iterative expansion, with the *z*-midplane cross-sectional shapes scoring close to the median value of *e* within each hydrogel group. Scale bars, 100 nm. Bottom, eccentricity values of HSV-1 virion *z*-midplane cross-sections for TG- and PAAG-based iterative expansion ($p = 6.3 \times 10^{-6}$, two-sided Wilcoxon rank sum test; TG, $n = 141$; PAAG, $n = 147$ virions; virions from the same single batch of live HSV-1 preparation). **b**, Top, schematic examples of shapes with sphericity (*s*) values of ~0.8, 0.7 and 0.6. Middle, HSV-1 virions expanded by TG- (top row) and PAAG-based (bottom row) two-round iterative expansion, with the *z*-midplane cross-sectional shapes scoring close to the median value of *s* within each hydrogel group. Scale bars, 100 nm. Bottom, sphericity values of HSV-1 virion *z*-midplane cross-sections for TG- and PAAG-based iterative expansion ($p = 8.9 \times 10^{-26}$, two-sided Wilcoxon rank sum test; TG, $n = 186$; PAAG, $n = 190$ virions; virions from the same single batch of live HSV-1 preparation). **c**, Top, schematic examples of shapes with normalized circular standard deviation (σ_n) values of ~0.05, 0.1 and 0.2. Middle, HSV-1 virions expanded by TG- (top row) and PAAG-based (bottom row) two-round iterative expansion, with the *z*-midplane cross-sectional shapes scoring close to the median value of σ_n within each hydrogel group. Scale bars, 100 nm. Bottom, normalized circular standard deviation values of HSV-1 virion *z*-midplane cross-sections for TG- and PAAG-based iterative expansion ($p = 1.5 \times 10^{-26}$, two-sided Wilcoxon rank sum test; TG, $n = 186$; PAAG, $n = 190$ virions; virions from the same single batch of live HSV-1 preparation). In **a**–**c**, data are presented as box plots, where the ends of the whiskers represent the maximum and minimum values of the distribution after outlying points (values above the 75th percentile + 1.5 × interquartile range, or below the 25th percentile − 1.5 × interquartile range) have been excluded, and where the upper line of the box represents the 75th percentile, the middle line represents the 50th percentile (median), the lower line represents the 25th percentile and the plus signs represent the individual values of the outlying points.

cross-sectional shapes using key shape descriptors, such as the eccentricity (*e*), the ratio of the minor axis to the major axis ($e = 1$ for a perfect circle; see the upper sketches in Fig. 5a for examples of shapes with different *e* values), the sphericity (*s*), the ratio of the radius of the inscribing circle to the radius of the circumscribing circle ($s = 1$ for a perfect circle; see the upper sketches in Fig. 5b for examples of shapes with different *s* values), and the normalized circular standard deviation (σ_n), the standard deviation of the eight radii within each particle divided by the mean for that particle ($\sigma_n = 0$ for a perfect circle; see the upper sketches in Fig. 5c for examples of shapes with different σ_n values). We found that the TG-expanded virions were significantly closer to circular compared with the PAAG-expanded virions ($p < 10^{-5}$ for all the descriptors, two-sided Wilcoxon rank sum test; Fig. 5). The changes were not small: the median deviation from a perfect circle was substantially reduced for TG compared with PAAG, by 62% (*e*), 64% (*s*) and 59% (σ_n) of the PAAG deviation. We applied the same shape analysis to the HIV virions and obtained data consistent with the HSV-1 values (Supplementary Fig. 6). In the future, even higher expansion factors, potentially revealing individual proteins on the virions, may be possible by expanding ~40× via three rounds of iterative expansion, with the initial expansion round being TG-based and the final two rounds being PAAG-based (Supplementary Fig. 8 and Supplementary Video 1).

Conclusions

We have found that TG polymers, assembled via non-radical step-growth polymerization of tetrahedral monomers, are capable of mediating ExM. When TG-based iterative expansion protocols were compared with classical PAAG-based protocols, using HSV-1 virion envelope proteins as the assay, we saw a reduction in spatial errors introduced by the expansion process, from 14.3 to 9.2 nm at the individual particle level. Using multiple classical shape descriptors such as ellipticity and sphericity to capture the improvements of TG over PAAG, we also found that TG-based iExM better retained the nanoscale shape of the HSV-1 virion envelope. Thus, TG-based ExM may overcome the local anisotropy of the expansion process that is inherent in previously used methods, and it may enable expansion with better preserved nanoscale morphology and shape. The single-digit distortions introduced by TG-based ExM raise the tantalizing question of whether new hydrogel chemistries may be able to achieve expansion accuracy approaching that of the size of individual biomolecules such as proteins.

Our current study is focused on the design principles of the hydrogel matrices for ExM, and it is not yet a protocol for general scientific use. For TG-based ExM to be useful in everyday scientific investigations, a number of improvements will be required. The chemicals must be made broadly available, through commercialization or other arrangements. Biomolecules of interest are currently anchored to the ends of monomers when incorporated into the hydrogel network, meaning that every anchored biomolecule results in a 'defect' in the polymer network because it terminates one of the monomer's arms; replacing such terminal-based anchoring with sidechain-based anchoring may improve TG structural homogeneity for ExM further. The ideal size of the monomer has not yet been established: current TG-based ExM monomers are much larger than the sodium acrylate monomers used in classical ExM protocols, raising the question of whether smaller TG monomers would better permeate dense cells and tissues. Finally, appreciation of the improvements offered by TG over PAAG will most likely require post-expansion antibody staining, or the use of very small tags such as nanobodies for pre-expansion staining, since the improvements offered by TG are smaller than the sizes of antibodies. To enable post-expansion antibody staining, the disulfide in the monomer will need to be replaced by a cleavable moiety that is compatible with the high-temperature treatments, basic pH environments and other conditions typically used to denature proteins and expand them away from each other[4,8,11]. For this approach, intramolecular epoxide cross-linking might be helpful for epitope preservation[46]. In the future, such a second-generation TG-based ExM process may be useful for investigating the detailed nanoscale spatial arrangement of molecular species in complexes, in cells and tissues, and in healthy and disease states.

Online content

Any methods, additional references, Nature Research reporting summaries, source data, extended data, supplementary information, acknowledgements, peer review information; details of author contributions and competing interests; and statements of data and code availability are available at https://doi.org/10.1038/s41565-021-00875-7.

Received: 18 November 2019; Accepted: 11 February 2021;
Published online: 29 March 2021

References

1. Chen, F., Tillberg, P. W. & Boyden, E. S. Expansion microscopy. *Science* **347**, 543–548 (2015).
2. Gao, R., Asano, S. M. & Boyden, E. S. Q&A: expansion microscopy. *BMC Biol.* **15**, 50 (2017).
3. Wassie, A. T., Zhao, Y. & Boyden, E. S. Expansion microscopy: principles and uses in biological research. *Nat. Methods* **16**, 33–41 (2019).
4. Asano, S. M. et al. Expansion microscopy: protocols for imaging proteins and RNA in cells and tissues. *Curr. Protoc. Cell Biol.* **80**, e56 (2018).
5. Hafner, A. S., Donlin-Asp, P. G., Leitch, B., Herzog, E. & Schuman, E. M. Local protein synthesis is a ubiquitous feature of neuronal pre- and postsynaptic compartments. *Science* **364**, eaau3644 (2019).
6. Schlichting, M. et al. Light-mediated circuit switching in the *Drosophila* neuronal clock network. *Curr. Biol.* **29**, 3266–3276.e3 (2019).
7. Zhao, Y. et al. Nanoscale imaging of clinical specimens using pathology-optimized expansion microscopy. *Nat. Biotechnol.* **35**, 757–764 (2017).
8. Tillberg, P. W. et al. Protein-retention expansion microscopy of cells and tissues labeled using standard fluorescent proteins and antibodies. *Nat. Biotechnol.* **34**, 987–992 (2016).
9. Chozinski, T. J. et al. Expansion microscopy with conventional antibodies and fluorescent proteins. *Nat. Methods* **13**, 485–488 (2016).
10. Chen, F. et al. Nanoscale imaging of RNA with expansion microscopy. *Nat. Methods* **13**, 679–684 (2016).
11. Ku, T. et al. Multiplexed and scalable super-resolution imaging of three-dimensional protein localization in size-adjustable tissues. *Nat. Biotechnol.* **34**, 973–981 (2016).
12. Gambarotto, D. et al. Imaging cellular ultrastructures using expansion microscopy (U-ExM). *Nat. Methods* **16**, 71–74 (2019).
13. Gao, R. et al. Cortical column and whole-brain imaging with molecular contrast and nanoscale resolution. *Science* **363**, eaau8302 (2019).
14. Chang, J.-B. et al. Iterative expansion microscopy. *Nat. Methods* **14**, 593–599 (2017).
15. Truckenbrodt, S. et al. X10 expansion microscopy enables 25 nm resolution on conventional microscopes. *EMBO Rep.* **19**, e45836 (2018).
16. Cohen, Y., Ramon, O., Kopelman, I. J. & Mizrahi, S. Characterization of inhomogeneous polyacrylamide hydrogels. *J. Polym. Sci. B Polym. Phys.* **30**, 1055–1067 (1992).
17. Yazici, I. & Okay, O. Spatial inhomogeneity in poly(acrylic acid) hydrogels. *Polymer* **46**, 2595–2602 (2005).
18. Orakdogen, N. & Okay, O. Correlation between crosslinking efficiency and spatial inhomogeneity in poly(acrylamide) hydrogels. *Polym. Bull.* **57**, 631–641 (2006).
19. Di Lorenzo, F. & Seiffert, S. Nanostructural heterogeneity in polymer networks and gels. *Polym. Chem.* **6**, 5515–5528 (2015).
20. Gu, Y., Zhao, J. & Johnson, J. A. A (macro)molecular-level understanding of polymer network topology. *Trends Chem.* **1**, 318–334 (2019).
21. Martens, P. & Anseth, K. S. Characterization of hydrogels formed from acrylate modified poly(vinyl alcohol) macromers. *Polymer* **41**, 7715–7722 (2000).
22. Lutolf, M. P. & Hubbell, J. A. Synthesis and physicochemical characterization of end-linked poly(ethylene glycol)-co-peptide hydrogels formed by Michael-type addition. *Biomacromolecules* **4**, 713–722 (2003).
23. Malkoch, M. et al. Synthesis of well-defined hydrogel networks using Click chemistry. *Chem. Commun.* 2774–2776 (2006).
24. Sakai, T. et al. Design and fabrication of a high-strength hydrogel with ideally homogeneous network structure from tetrahedron-like macromonomers. *Macromolecules* **41**, 5379–5384 (2008).
25. Fairbanks, B. D. et al. A versatile synthetic extracellular matrix mimic via thiol-norbornene photopolymerization. *Adv. Mater.* **21**, 5005–5010 (2009).
26. Cui, J. et al. Synthetically simple, highly resilient hydrogels. *Biomacromolecules* **13**, 584–588 (2012).
27. Saffer, E. M. et al. SANS study of highly resilient poly(ethylene glycol) hydrogels. *Soft Matter* **10**, 1905–1916 (2014).
28. Matsunaga, T., Sakai, T., Akagi, Y., Chung, U.-i. & Shibayama, M. Structure characterization of Tetra-PEG gel by small-angle neutron scattering. *Macromolecules* **42**, 1344–1351 (2009).
29. Matsunaga, T., Sakai, T., Akagi, Y., Chung, U.-i. & Shibayama, M. SANS and SLS studies on tetra-arm PEG gels in as-prepared and swollen states. *Macromolecules* **42**, 6245–6252 (2009).
30. Oshima, K., Fujimoto, T., Minami, E. & Mitsukami, Y. Model polyelectrolyte gels synthesized by end-linking of tetra-arm polymers with click chemistry: synthesis and mechanical properties. *Macromolecules* **47**, 7573–7580 (2014).
31. Kamata, H., Akagi, Y., Kayasuga-Kariya, Y., Chung, U.-i. & Sakai, T. "Nonswellable" hydrogel without mechanical hysteresis. *Science* **343**, 873–875 (2014).
32. Tricot, M. Comparison of experimental and theoretical persistence length of some polyelectrolytes at various ionic strengths. *Macromolecules* **17**, 1698–1704 (1984).
33. Kienberger, F. et al. Static and dynamical properties of single poly(ethylene glycol) molecules investigated by force spectroscopy. *Single Mol.* **1**, 123–128 (2000).
34. Kuhn, W. Über die Gestalt fadenförmiger Moleküle in Lösungen. *Kolloid Z.* **68**, 2–15 (1934).
35. Kuhn, W. & Kuhn, H. Die Frage nach der Aufrollung von Fadenmolekeln in strömenden Lösungen. *Helv. Chim. Acta* **26**, 1394–1465 (1943).

36. Debye, P. & Hückel, E. The theory of electrolytes. I. Lowering of freezing point and related phenomena. *Phys. Z.* **24**, 185–206 (1923).
37. Dommerholt, J., Rutjes, F. P. J. T. & van Delft, F. L. Strain-promoted 1,3-dipolar cycloaddition of cycloalkynes and organic azides. *Top. Curr. Chem.* **374**, 16 (2016).
38. Zander, Z. K., Hua, G., Wiener, C. G., Vogt, B. D. & Becker, M. L. Control of mesh size and modulus by kinetically dependent cross-linking in hydrogels. *Adv. Mater.* **27**, 6283–6288 (2015).
39. Hughes, M. P., Morgan, H. & Rixon, F. J. Dielectrophoretic manipulation and characterization of herpes simplex virus-1 capsids. *Eur. Biophys. J.* **30**, 268–272 (2001).
40. Liu, F. & Zhou, Z. H. in *Human Herpesviruses: Biology, Therapy, and Immunoprophylaxis* (eds Arvin, A. et al.) 27–43 (Cambridge Univ. Press, 2007).
41. Brown, J. C. & Newcomb, W. W. Herpesvirus capsid assembly: Insights from structural analysis. *Curr. Opin. Virol.* **1**, 142–149 (2011).
42. Grünewald, K. et al. Three-dimensional structure of herpes simplex virus from cryo-electron tomography. *Science* **302**, 1396–1398 (2003).
43. Maurer, U. E., Sodeik, B. & Grünewald, K. Native 3D intermediates of membrane fusion in herpes simplex virus 1 entry. *Proc. Natl Acad. Sci. USA* **105**, 10559–10564 (2008).
44. Laine, R. F. et al. Structural analysis of herpes simplex virus by optical super-resolution imaging. *Nat. Commun.* **6**, 5980 (2015).
45. Liu, J., Wright, E. R. & Winkler, H. in *Cryo-EM, Part C: Analyses, Interpretation, and Case studies* Vol. 483 (ed. Jensen, G. J.) 267–290 (Academic, 2010).
46. Park, Y.-G. et al. Protection of tissue physicochemical properties using polyfunctional crosslinkers. *Nat. Biotechnol.* **37**, 73–83 (2019).

Methods

Synthesis of TG monomers. Monomer **1** was synthesized using a procedure modified from a previously described synthesis (Supplementary Fig. 1)[30]. First, tetra-arm poly(*t*-butyl acrylate) with bromo terminal groups (**4**) was synthesized by atom transfer radical polymerization. Next, tetra-arm poly(*t*-butyl acrylate) with azide terminal groups (**5**) was synthesized by replacing the bromo groups of **4** with azides (Supplementary Fig. 2). Finally, monomer **1** was synthesized by hydrolysis and neutralization of **5** to a final pH ≈ 7. Monomers **2′**, **2″** and **2‴** were synthesized by NHS ester-based conjugation of the alkynes (DBCO-NHS, BCN-NHS or DBCO-SS-NHS) to the terminal primary amines of the tetra-arm PEGs. A detailed procedure for the synthesis can be found in the Supplementary Methods.

Cell culture. HEK293FT cells (Thermo Fisher) were cultured in chambered coverglasses (CultureWell, Thermo Fisher) to a confluency of 60–80% (ref. [1]), before being fixed and immunostained[1,4,8]. Briefly, the cells were treated with 3% (w/v) formaldehyde and 0.1% (w/v) glutaraldehyde in phosphate buffered saline (PBS; 1× unless otherwise noted) for 10 min at room temperature before the subsequent quenching, blocking, immunostaining and expansion procedures. HeLa cells (ATCC CCL-2) were plated on coverglasses coated with Matrigel (BD Sciences) to a confluency of 50–90% and fixed[1,4,8,14]. The cells were treated with PBS with 3% (w/v) formaldehyde and 0.1% (w/v) glutaraldehyde for 10 min at room temperature before the subsequent quenching, blocking and expansion procedures. All of the cells were not subjected to additional authentication and were not tested for mycoplasma contamination. A detailed procedure for the immunostaining can be found in the Supplementary Methods.

Thy1-YFP mouse brain slice. All procedures involving Thy1-YFP-H transgenic mice (Jackson Laboratory) were performed in accordance with the US National Institutes of Health Guide for the Care and Use of Laboratory Animals and approved by the MIT Committee on Animal Care. All of the animals were housed in groups in standardized cages (temperature: 20–22 °C, humidity: 30–70%) with a 12-hour light/12-hour dark cycle with unrestricted access to food and water. Coronal brain slices (50–100 μm) of Thy1-YFP-H mice of 2–4 months old, both male and female, were prepared and immunostained for expansion[4,8,13]. A detailed procedure for the immunostaining can be found in the Supplementary Methods.

General procedure for gelation, digestion and expansion. Fixed (and immunostained) cells and tissues were incubated in ~0.1–0.2 mg ml^{-1} NHS-azide in PBS overnight at room temperature and washed with PBS twice. To form the gelling solution, the two monomer solutions were mixed at a close to 1:1 molar ratio and an additional amount of water was added to adjust the final concentration of monomer **1** to ~3.3% (w/v). For example, 10 μl each of monomers **1** and **2′** (both ~200 mg ml^{-1}) and 40 μl of water were mixed to yield the gelling solution. Gelation was carried out for 1–2 h at 37 °C (blank gels) or overnight at 4 °C (cell and tissue samples) in a gelation chamber[4,8]. The gelled cell and tissue samples were incubated in digestion buffer with proteinase K (8 units ml^{-1}, 1:100 dilution; New England BioLabs) overnight at room temperature[4,8] and expanded in an excess amount of water three times, each time for 20 min.

Expansion of HeLa cells (pre-expansion immunostaining and iterative expansion). Fixed HeLa cells were stained with primary antibodies, oligonucleotide-conjugated secondary antibodies and azide-modified tertiary oligonucleotides as previously described[1,14]. The cells were gelled with a cleavable TG gelling solution prepared by mixing monomers **1** and **2‴** with water. The gelled samples were incubated in digestion buffer with proteinase K (8 units ml^{-1}) overnight at room temperature with gentle shaking before de-hybridization of the oligonucleotides from the gel-anchored oligonucleotides. The expanded samples were re-embedded in *N*,*N*′-bis(acryloyl)cystamine (BAC)-cross-linked non-expanding gel, hybridized with first linker oligonucleotides, re-embedded in *N*,*N*′-diallyl L-tartardiamide (DATD)-cross-linked expanding gel, and incubated in BAC-cleaving buffer. For fluorescence readout, the samples were incubated with fluorophore-conjugated locked nucleic acid (LNA) oligonucleotides and expanded in water. A detailed procedure for the expansion can be found in the Supplementary Methods.

Expansion of HSV-1 virions (direct labelling and iterative expansion). Purified HSV-1 virion stock[47] was diluted before being drop-cast on to a plasma-cleaned #0 circular 12 mm coverslip. After 15 min of incubation at room temperature, the virions were fixed in 4% paraformaldehyde in PBS for 10 min. Azide-modified oligonucleotides were directly conjugated to the virion envelope proteins via SoluLink bioconjugation chemistry as previously described[1]. The virions were gelled, digested, expanded and hybridized with fluorophore-conjugated LNA oligonucleotides using a similar procedure to that used for the HeLa cell expansion. For three-round iterative expansion, BAC-cleaved samples were re-embedded in DATD-cross-linked non-expanding gel, hybridized with second linker oligonucleotides, re-embedded in bis-cross-linked expanding gel and incubated in DATD-cleaving buffer before hybridization with the LNA oligonucleotide, expansion and imaging. A detailed procedure for the expansion and for the PAAG control can be found in the Supplementary Methods.

Expansion of HIV and VSV virions (direct labelling and iterative expansion). Purified HIV and VSV virions were immobilized, fixed, conjugated with oligonucleotides, gelled and then expanded following the two-round iterative expansion protocol of the HSV-1 virions.

Imaging and visualization. All the expanded samples were imaged with a diffraction-limited spinning disk confocal microscope (CSU-W1, Yokogawa on Eclipse Ti-E microscope body; Nikon) with a CFI Apo LambdaS LWD ×40, 1.15 NA water-immersion objective (Nikon), controlled using NIS-Elements AR imaging software, v4.60.00 (Nikon). The two-colour HeLa cell images and all the virion images were deconvolved using theoretical point-spread-functions (Huygens Essential for MacX11 built on 7 Feb 2013; SVI) before visualization and image analysis. Unless otherwise noted, all the three-dimensional (3D) renderings were generated using Imaris ×64 8.3 (Oxford Instruments). Part of the image datasets was analysed and visualized using ImageJ (Fiji) 2.10/1.53c. Part of the plots was generated using OriginPro8.1 (Origin).

Image analysis. For virion envelope protein analysis, first, single-particle averaged virion images were generated using a semi-automated image analysis pipeline[48] implemented on MATLAB R2018a-R2020b. Each virion was manually aligned, automatically cropped, calibrated with the expansion factor and arithmetically averaged to generate the single-particle averaged images. Next, spatial arrangements of the virion envelope proteins were quantified. Radii in eight directions (45° apart) were measured for each virion as the distance from the particle centroid to the Gaussian-fitted centre of the envelope profile. After inspection to remove unfitted profiles, standard deviations of all the accepted radii within the same particle (σ) were reported as population statistics for virions with ≥3 accepted radii. For HSV-1 virion shape analysis, virions with ≥6 accepted radii (for eccentricity measurements, virions with ≥6 accepted radii and with the accepted radii constituting at least two mutually perpendicular diameters) were used to assure an accurate approximation of the particle shapes. The eccentricity (e) was defined as the ratio of the minor axis to the major axis. The sphericity (s) was defined as the ratio of the radius of the inscribing circle to the radius of the circumscribing circle. The normalized circular standard deviation (σ_n) was defined as the standard deviation of normalized radii (R_n) within each particle. For microtubule analysis, the peak-to-peak distance between the microtubule sidewalls was measured using a semi-automated algorithm[49] implemented on MATLAB R2018a-R2020b. On maximum intensity z-projection images of β-tubulin-stained HeLa cells, two points were manually selected along the centreline of a microtubule segment and a 200 nm (in biological length) segment was cropped out from the selected segment. The line intensity profile along the 200 nm segment was fitted with two Gaussian functions to detect the two peaks in the fluorescence intensity, between which the distance was measured as the peak-to-peak distance of the microtubule sidewalls. A detailed description of the image analysis can be found in the Supplementary Methods.

Modelling and simulation of single-particle averaged HSV-1 virion images. A model of spherical virions was developed on MATLAB R2020a-R2020b based on experimental parameters derived from individual HSV-1 virions, to simulate the single-particle averaged HSV-1 virion images[50] and their quantitative metrics. A detailed description of the modelling can be found in the Supplementary Methods.

Reporting Summary. Further information on research design is available in the Nature Research Reporting Summary linked to this article.

Data availability

Source data are provided with this paper. The total raw data size of the study exceeds 350 GB. The data that support this study are available from the authors upon reasonable request.

Code availability

Analysis code used in this study, including virus particle analysis[48], microtubule peak-to-peak distance analysis[49] and HSV-1 averaged particle image simulation[50] are available at https://github.com/jayyu0528/.

References

47. Neve, R. L., Neve, K. A., Nestler, E. J. & Carlezon, W. A. Use of herpes virus amplicon vectors to study brain disorders. *Biotechniques* **39**, 381–391 (2005).
48. Yu, C.-C. Virus particle analysis. *Github* https://github.com/jayyu0528/(2020).
49. Yu, C.-C. Microtubule peak-to-peak distance analysis. *Github* https://github.com/jayyu0528/ (2020).
50. Yu, C.-C. HSV-1 averaged particle image simulation. *Github* https://github.com/jayyu0528/ (2020).

Acknowledgements

We thank Y.-Y. Chou and T. Kirchhausen at HMS for help with VSV stock preparation and virion immobilization; C. Linghu and O. Shemesh for help with HSV-1 stock preparation; P. Valdes and C. Zhang for helpful discussion about sample staining

and expansion; M. J. Kauke for helpful discussion about DNA staining; S. M. Asano for helpful discussion about image analysis; G. H. Huynh for help with mouse brain slice preparation; F. Chen for helpful discussion about monomer and polymerization chemistry design; R. Herlo at HMS for helpful discussion about virion envelope proteins. E.S.B. acknowledges L. Yang and Y. E. Tan, J. Doerr, the Open Philanthropy Project, NIH 1R01NS087950, NIH 1RM1HG008525, NIH 1R01DA045549, NIH 2R01DA029639, NIH 1R01NS102727, NIH 1R01EB024261, NIH 1R01MH110932, the HHMI-Simons Faculty Scholars Program, the HHMI Investigator program, IARPA D16PC00008, the US Army Research Laboratory and the US Army Research Office under contract/grant W911NF1510548, the US–Israel Binational Science Foundation Grant 2014509, NSF Grant 1734870 and the NIH Director's Pioneer Award 1DP1NS087724. C.-C.Y. acknowledges the McGovern Institute for Brain Research at MIT for the Friends of the McGovern Fellowship. S.U. was supported by Biogen and NIH 5R01GM075252-13S grants awarded to T. Kirchhausen, and acknowledges support from Philomathia Foundation and Chan Zuckerberg Initiative Imaging Scientist program.

Author contributions

R.G. and L.G. designed and synthesized the monomers and conducted initial gelation experiments. C.-C.Y. and R.G. designed and conducted iterative expansion, virion expansion and associated analysis. C.-C.Y. created the semi-automated virion analysis pipeline and the simulation model. K.D.P. helped characterization of the gel in cell culture. R.L.N. purified HSV-1 and prepared the virion stock solution. J.B.M. provided purified HIV virions. S.U. provided purified VSV virions and conducted initial virion immobilization experiments. C.-C.Y., R.G. and L.G. processed and performed quantitative analysis of all image data. R.G., C.-C.Y. and E.S.B. wrote the manuscript with input from all co-authors. E.S.B. supervised the project.

Competing interests

R.G., C.-C.Y., L.G. and E.S.B. have filed for patent protection on a subset of the technologies here described. E.S.B. is a cofounder of a company that aims to commercialize ExM for medical purposes. R.G., C.-C.Y., L.G. and E.S.B. are co-inventors on multiple patents related to ExM. The authors declare no other competing interests.

Additional information

Supplementary information The online version contains supplementary material available at https://doi.org/10.1038/s41565-021-00875-7.

Correspondence and requests for materials should be addressed to E.S.B.

Peer review information *Nature Nanotechnology* thanks the anonymous reviewers for their contribution to the peer review of this work.

Reprints and permissions information is available at www.nature.com/reprints.